Aerodynamic probe calibration using Gaussian process regression

OPEN ACCESS
IOP Publishing
Measurement Science and Technology
Meas. Sci. Technol. **31** (2020) 125301 (16pp)
https://doi.org/10.1088/1361-6501/aba37d

Aerodynamic probe calibration using Gaussian process regression

Florian M Heckmeier and Christian Breitsamter

Chair of Aerodynamics and Fluid Mechanics, Department of Mechanical Engineering, Technical University of Munich, 85748 Garching bei München, Germany

E-mail: florian.heckmeier@aer.mw.tum.de

Received 14 April 2020, revised 25 June 2020
Accepted for publication 7 July 2020
Published 30 September 2020

Abstract

During the calibration of an aerodynamic probe, the correlation between the present representative flow quantities of the fluid and the measurand is determined. Thus, a large number, sometimes several thousands, of different calibration points are set and measured, making this a very time-consuming process. The differences in the calibration data of similar constructed probes are very small. With the help of statistical methods, more precisely Gaussian process regressions, this similarity is exploited in order to use existing calibration data of different probes reducing the calibration time with sufficient reconstruction accuracy. Data from single-wire hot-wire probes and from five-hole probes are tested and show a very high reconstruction accuracy compared to the full calibration data set. The number of calibration points in the five-hole probe case is reduced by at least one order of magnitude with comparable reconstruction accuracy.

Keywords: aerodynamic intrusive measurement, probe calibration, gaussian process regression, machine learning, multi-hole pressure probe, constant temperature anemometry (CTA)

(Some figures may appear in colour only in the online journal)

1. Introduction

Experimentally obtained data of flow phenomena are still of great interest for academic and industrial research, despite the ongoing development and optimization of CFD (computational fluid dynamics) simulations. Furthermore, experimental results often serve as data basis for the validation of CFD solvers. The most commonly used intrusive measurement methods are hot-wire probes and multi-hole pressure probes. Even though hot-wire constant temperature anemometry (CTA) is known for its high temporal resolution, hot-wire probes are characterized by very low mechanical robustness when used in harsh environments. In contrast, multi-hole pressure probes are inexpensive to manufacture and easy to operate. However, attention should be paid to the fact that meaningful and accurate measurement results can only be obtained if the probe has been calibrated under representative conditions before use. During the calibration, different combinations of flow parameters (inflow velocity and flow angles) are set in a calibration free-jet wind tunnel [1, 2]. The corresponding measurement data are recorded with the aerodynamic measurement probe. Depending on the probe and the expected reconstruction accuracy, this calibration process sometimes comprises several hundreds or thousands of calibration points [3]. Thus, the calibration is a very time-consuming step. Hot-wire probes for example require a recalibration before each measurement campaign or after damage to the wire and rewelding.

When analyzing the calibration data, it is noteworthy that the (multivariate) functions are often very alike in shape. Since aerodynamic probe calibrations can be described as regression problems, besides a standard polynomial regression approach, Bayesian statistics methods can be used. Gelman *et al* describe

the basics of Bayesian statistics [4]. Furthermore, Rasmussen applies *Gaussian processes* $\mathcal{GP}$ to machine learning problems, both for regression and classification problems [5]. In various research fields in the literature, Gaussian processes have been applied: in geostatistics, Gaussian process regression is better known as *kriging* [6]. During the application of $\mathcal{GP}$s, the placement of test point locations is crucial. Krause *et al* describe an optimization routine for the placement of the locations in Gaussian process problems [7]. Furthermore, in engineering applications, Gaussian process regression has been used for the wind energy turbine power curve model prediction [8]. Its application on the calibration of spectroscopic sensors has also been shown [9]. In aerodynamic metrology, Garcia-Ruiz *et al* show the application of Gaussian processes for the hot-wire temperature compensation [10]. Moreover, Agrawal *et al* introduce a non-linear regression approach to minimize recalibration for non-thermal drifts [11].

Since aerodynamic probe calibrations a) require a regression within all measured data points, and b) show similarity among themselves, the idea of applying Bayesian statistics, viz. Gaussian process regression, on aerodynamic probe calibration arises. Hence, governing hypotheses can be identified and are investigated within this paper:

Hypothesis 1 *The knowledge of former calibration data of various different shaped probes can be transferred to future probe calibrations incorporating the similarity among themselves.*

Hypothesis 2 *Bayesian statistics and machine learning algorithms, more precisely Gaussian process regression, are applicable on aerodynamic probe calibration data.*

Hypothesis 3 *The number of calibration points needed can be significantly reduced while still showing acceptable reconstruction accuracy, and thus, leading to a reduction of time consumption.*

Especially under the assumption that the first two hypotheses hold, a confirmation of the third hypothesis could result in a significant time saving in set-up costs of a measurement campaign with aerodynamic probes.

In this paper, the usage of Gaussian process regression for the reduction of calibration points is described. Hence, the theoretical background of Gaussian processes is outlined first in section 2. Moreover, the calibration process for hot-wire anemometry and multi-hole pressure probes is described in section 3. In the last part of the paper (see section 4), investigations on the applicability of the Gaussian process regression on real calibration data is demonstrated. The procedure is introduced with a generic example. Furthermore, apart from single-wire hot-wire data, the focus lies on the application of Gaussian process regression on the calibration of multi-hole pressure probes. Thereby, several $\mathcal{GP}$s have to be considered simultaneously side by side.

2. Gaussian process regression

In this section, the theoretical background to Gaussian process regression is explained. In section 2.1, the principles of Bayesian statistics are outlined. The theory of the Gaussian process regression is introduced in section 2.2. The upcoming sections are based on the more detailed discussion given by Rasmussen and Williams by addressing Gaussian processes in machine learning applications [5, 12]. Furthermore, general information on pattern recognition and machine learning is given by Bishop [13].

2.1. Theoretical background to Bayesian statistics

Engineering problems are often characterized by the lack of available information. This is where probability models provide a remedy when it comes to dealing with the challenge of missing information. In Bayesian statistics, the model based on existing data can successively be improved with new information by inference. The question on how probabilities change due to new information are thus brought into a mathematical framework by using the Bayesian theorem. The more general question on what can be inferred on the population based on samples is hereby answered. Hence, the Bayesian formalism introduces various probabilities, which are described in the following: A *prior* probability $P(H)$ has to be specified, expressing the belief about the hypothesis before incorporating observations. The *likelihood* probability $P(E|H)$ is the probability of the observations given the hypothesis. The *marginal likelihood* or evidence $P(E)$ is the normalizing constant. The *posterior* combines the likelihood and the prior and takes all information that is known into account. The posterior $P(H|E)$, the probability of the hypothesis given the evidence, can be calculated by Bayes' rule:

$$posterior = \frac{likelihood \times prior}{marginal\ likelihood} \tag{1}$$

$$P(H|E) = \frac{P(E|H) \times P(H)}{P(E)} \tag{2}$$

2.2. Gaussian processes

In the context of Bayesian statistics, multiple machine learning algorithms have been developed, one of which is the Gaussian process regression. As noted in the Bayesian statistics introducing comments, new information can be used to infer a new posterior Gaussian process model, which incorporates the observations by updating the initial/prior Gaussian process. In contrast to basic fitting methods, the expected order of the approximation does not need to be specified beforehand for the Gaussian process regression.

A Gaussian process describes a distribution over functions and is fully characterized by the mean function $m(\mathbf{x})$ and the covariance function $k(\mathbf{x}, \mathbf{x}')$ of a real process $f(\mathbf{x})$.

$$m(\mathbf{x}) \quad = \mathbb{E}[f(\mathbf{x})] \tag{3}$$

$$k(\mathbf{x}, \mathbf{x}') \quad = \mathbb{E}[(f(\mathbf{x}) - m(\mathbf{x}))(f(\mathbf{x}') - m(\mathbf{x}'))] \tag{4}$$

For noise-free observations, the Gaussian process can be written as:

$$f(\mathbf{x}) \sim \mathcal{GP}(m,k) \tag{5}$$

A distinct finite number n of locations is considered further and the mean μ and the covariance Σ can be expressed as:

$$\mu_i = m(x_i), \qquad i = 1,\ldots,n \tag{6}$$

$$\Sigma_{ij} = k(x_i,x_j), \qquad i,j = 1,\ldots,n \tag{7}$$

The joint distribution of n known training case function values, $\mathbf{f}$, and a set of n_* function values corresponding to the test set inputs, $\mathbf{f}_*$, gives:

$$\begin{bmatrix} \mathbf{f} \\ \mathbf{f}_* \end{bmatrix} \sim \mathcal{N}\left(\begin{bmatrix} \boldsymbol{\mu} \\ \boldsymbol{\mu}_* \end{bmatrix}, \begin{bmatrix} \Sigma_{\mathbf{f},\mathbf{f}} & \Sigma_{\mathbf{f},*} \\ \Sigma_{*,\mathbf{f}} & \Sigma_{*,*} \end{bmatrix} \right) \tag{8}$$

Here, for example $\Sigma_{\mathbf{f},*} = \Sigma(X,X_*)$ represents the $n \times n_*$ matrix of the covariances evaluated at all n training points X and n_* test points X_*.

The predictive joint posterior distribution can be used to sample function values $\mathbf{f}_*$ of test inputs X_* by evaluating the mean and covariance matrix:

$$(\mathbf{f}_*|X_*,X,\mathbf{f}) \sim \mathcal{N}\Big(\boldsymbol{\mu}_* + \Sigma_{*,\mathbf{f}}\Sigma_{\mathbf{f},\mathbf{f}}^{-1}(\mathbf{f}-\boldsymbol{\mu}), \Sigma_{*,*} - \Sigma_{*,\mathbf{f}}\Sigma_{\mathbf{f},\mathbf{f}}^{-1}\Sigma_{\mathbf{f},*}\Big) \tag{9}$$

The covariance of a Gaussian process random variable can be described by the *kernel* or *covariance function* and relates one observation to another. For a valid kernel function, the kernel matrix $\Sigma = k(X,X)$ has to be positive definite. This implies a symmetric covariance matrix. The prediction of the Gaussian process strongly depends on the choice of the covariance function. Instead of fixing it to a specific shape, usually a parametric family of functions is selected and its parameters are optimized by inferring with the training data. In the following, two different families are introduced. Afterwards, it is shown briefly how the *hyperparameters* can be optimized.

2.2.1. Kernel function families. One of the most basic kernel function families is the squared exponential kernel, or Gaussian kernel (see figure 1 (top)):

$$k(\mathbf{x},\mathbf{x}') = \sigma_f^2 \exp\left(-\frac{\|\mathbf{x}-\mathbf{x}'\|_2^2}{2\sigma_l^2}\right) \tag{10}$$

Here, σ_f denotes the signal standard deviation or the maximum allowable covariance between two different observations. Further, σ_l is the characteristic length scale which defines the range of influence of two different observations. Another kernel function, which is commonly applied, is the Matérn 3/2 covariance function (see figure 1 (bottom)). This kernel function is also used for the $\mathcal{GP}$ of the CTA and the multi-hole pressure probe data in section 4.2 and 4.3, respectively:

$$k(\mathbf{x},\mathbf{x}') = \sigma_f^2(1+\sqrt{3}r)\exp\left(-\sqrt{3}r\right), \text{with } r = \frac{\|\mathbf{x}-\mathbf{x}'\|_2}{\sigma_l} \tag{11}$$

Figure 2 shows a representation of the kernel matrix for both the Gaussian and the Matérn 3/2 kernels with randomly chosen hyperparameters $\sigma_f = 1.0$ and $\sigma_l = 1.0$. Comparing both kernel functions, it can be seen that the squared exponential kernel shape has a broader peak in comparison to the Matérn kernel, but contrary flattens out earlier with increasing distance $\|\mathbf{x}-\mathbf{x}'\|_2$.

The set of hyperparameters is often pooled in the vector $\boldsymbol{\theta}$. For the previously defined kernel functions, $\boldsymbol{\theta}$ is defined as:

$$\boldsymbol{\theta} = \begin{pmatrix} \theta_1 \\ \theta_2 \end{pmatrix} = \begin{pmatrix} \sigma_l \\ \sigma_f \end{pmatrix} \tag{12}$$

Depending on the mean and kernel function chosen in the prior step, different free parameters have to be set. The stated equations hold true for noise-free data. In real-world problems, observations are subject to noise. This can be expressed in additional terms in the $\mathcal{GP}$ formulation. The measured value $\mathbf{y}$ with noise is defined as: $\mathbf{y} = \mathbf{f}(\mathbf{x}) + \epsilon$. Here, the noise ε is Gaussian distributed with a noise variance σ_n^2. Furthermore, the covariance also changes to $\Sigma_y = \Sigma_f + \sigma_n^2 I$, where Σ_f is the covariance matrix for noise-free observations.

2.2.2. Training of hyperparameters. The evaluation of the marginal likelihood function $p(\mathbf{y}|X,\boldsymbol{\theta})$ is the basis for the training of the hyperparameter vector $\boldsymbol{\theta}$. This can be done by maximizing the log likelihood function with efficient gradient-based algorithms, e.g. conjugate gradient solvers [14]. The log likelihood function $\mathcal{L}$ for multivariate Gaussian distributions is given by:

$$\mathcal{L} = \log p(\mathbf{y}|X,\boldsymbol{\theta}) = -\frac{1}{2}\mathbf{y}^T\Sigma_y^{-1}\mathbf{y} - \frac{1}{2}\log|\Sigma_y| - \frac{n}{2}\log 2\pi. \tag{13}$$

It has to be noted that $\log p(\mathbf{y}|X,\boldsymbol{\theta})$ is a non-convex function. Hence, it could have multiple maxima. Numerous methods in the literature cover the determination and optimization of this problems by inverting Σ_y efficiently while reducing computational costs of the $\mathcal{O}(n^3)$ computation.

Furthermore, regarding non-linear optimization, the gradient of the log likelihood function is needed as well. This is done by seeking the partial derivatives of the marginal likelihood w.r.t. the hyperparameters θ_j (here, Tr is the trace of the matrix):

$$\frac{\partial}{\partial\theta_j}\mathcal{L} = -\frac{1}{2}\mathrm{Tr}\left(\Sigma_y^{-1}\frac{\partial\Sigma_y}{\partial\theta_j}\right) + \frac{1}{2}\mathbf{y}^T\frac{\partial\Sigma_y}{\partial\theta_j}\Sigma_y^{-1}\mathbf{y}. \tag{14}$$

2.2.3. Sparse $\mathcal{GP}$ for large data sets. In the case of a high number of input/training data sets, $\mathcal{GP}$ models experience a high computational effort due to matrix inversions in the inference step. Considering n training points $\mathbf{x}$, an exact inference via the Gaussian likelihood method is of $\mathcal{O}(n^3)$ for the standard $n \times n$ matrix inversion. In order to reduce the computational load, there are different methods to approximate the covariance matrix. Instead of using the full covariance matrix Σ,

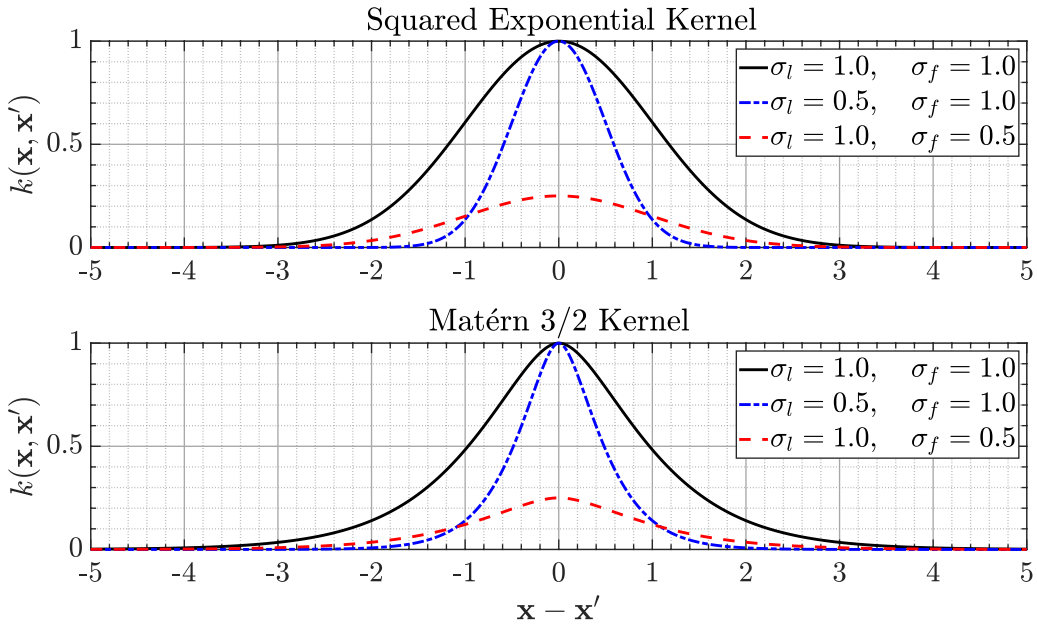

Figure 1. Squared exponential kernel (top) and Matérn kernel (bottom) for various hyperparameters σ_f and σ_l.

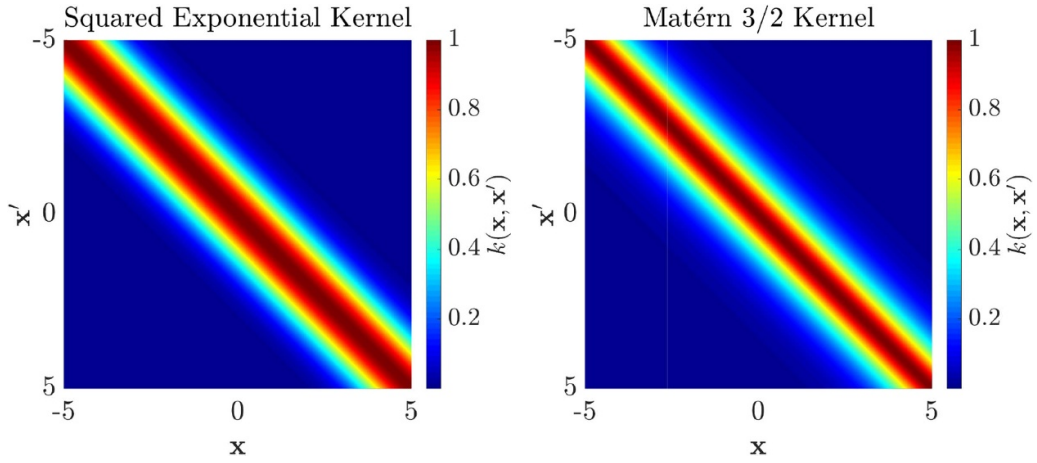

Figure 2. Squared exponential kernel matrix (left) and Matérn 3/2 kernel matrix (right) for hyperparameters $\sigma_f = 1.0$ and $\sigma_l = 1.0$.

an approximate matrix $\tilde{\Sigma}$ is used for the inference. Quinonero-Candela and Rasmussen give an overview of different methods [15]. Generally, the approximation methods work with a set of m inducing points $\mathbf{u}$ with a reduced computational load of $\mathcal{O}(mn^2)$. In the GPML Matlab toolbox the *Fully Independent Training Conditional (FITC)* approximation is applied, which is briefly explained in the following. The approximated covariance matrix $\tilde{\Sigma} \approx \Sigma$ can be expressed as [15–17]:

$$\tilde{\Sigma} = Q + G \tag{15}$$

with

$$G = diag(\Sigma - Q), \quad Q = \Sigma_u^T \, Q_{uu}^{-1} \, \Sigma_u,$$
$$Q_{uu} = \Sigma_{uu} + \sigma_{n_u}^2 I, \tag{16}$$

with σ_{n_u} being the noise variance from the inducing points. The diagonal matrix $diag(A)$ comprises the diagonal elements of A. Besides the known $n \times n$ covariance matrix Σ, the formula also uses the $n \times m$ covariance matrix between the test points and the inducing points Σ_u and the $m \times m$ covariance matrix between the inducing points Σ_{uu}.

3. Calibration of aerodynamic probes

The application of aerodynamic probes in experiments in unknown flow conditions requires a calibration of the probe in a known free-jet calibration wind tunnel in advance. Within the context of the aerodynamic/spatial calibration of a probe, the correlation between the mean free-jet flow conditions and the measured quantity $x_{meas,c}$ at the probe is determined. The index c denotes values in the calibration step, whereas the index T will be used for values in the reconstruction of test points. x_{meas} can, for example, be the voltage measured by a hot-wire probe or the pressure recorded by a multi-hole pressure probe at the location of its pressure transducer. During the calibration, different combinations of the free-jet velocity $U_{\infty,c}$ and

the flow angles α_c and β_c are set in the free-jet calibration wind tunnel, see figure 3. In order to determine the actual flow conditions at the probe tip in an experiment, the measurand $x_{meas,T}$ must be post-processed with the stored calibration data. In the literature, there are several methods how the calibration data can be used to reconstruct the flow field properties. The most commonly used one is an interpolation approach, which is applied to calculate the flow data at the probe tip based on the acquired measurements. In the following sections, the calibration and reconstruction methods for both measurements techniques, hot-wire anemometry in section 3.1 and multi-hole pressure probes in section 3.2, are briefly introduced.

3.1. Hot-wire probes

The calibration of a CTA hot-wire probe determines a relationship between the CTA output and the flow velocity U_∞. It is performed by exposing the probe to a known flow and recording the voltages E. A curve fit through the acquired points (E, U_∞) is used when converting data sets from voltages to velocities, see figure 4. CTA bases on the cooling effect of the flow on the wire (convective heat transfer). The current/voltage that has to be provided by the anemometer to the wire to keep the wire at a constant temperature is measured. The wire is one arm of a Wheatstone bridge and has to be balanced before being calibrated. Hence, the bridge voltage E is a direct measure for the flow velocity U_∞. Furthermore, it is important to monitor the air temperature during the probe calibration. If it varies from calibration to measurement, it is necessary to correct the CTA data for temperature variations, see [18–20]. The gold-plated tungsten wire with a length of approximately 1.25 *mm* and a diameter of 5 µm is welded between two prongs. The sensor temperature coefficient is 0.003 6 1 K^{-1} and an overheat ratio of $a = 1.8$ is applied within all calibrations. For X-wire or triple-wire probes, a directional calibration has to be performed. For reasons of brevity, this paper does not deal with the directional calibrations for hot-wire probes in detail. Henceforth, solely single-wire probes are considered. More details on multi-wire probes can be found in the literature [21]. For single-wire probes, the calibrated data points, shown in figure 4, can be approximated with either a polynomial or a power-law curve fitting:

$$U = a_0 + a_1 \cdot E + a_2 \cdot E^2 + a_3 \cdot E^3 + a_4 \cdot E^4 \tag{17}$$

$$E^2 = A + B \cdot U^n \tag{18}$$

Here, $\boldsymbol{\theta}_{poly} = [a_0, a_1, a_2, a_3, a_4]$ are calibration coefficients for the polynomial fit, whereas A and B and n represent the calibration constants for the power law fit $\boldsymbol{\theta}_{pow} = [A, B, n]$. The exponent n usually lies in the region of $n = (0.4, 0.55)$ and is adapted to the calibration data set.

3.2. Multi-hole pressure probes

The working principle of pressure probes relies on the stagnation of the flow around the probe. At the stagnation point, the total pressure p_t is equal to the sum of the static pressure p_s and the dynamic pressure q. Multi-hole probes measure the total pressure of the flow at various locations at the probe tip. By measuring all pressures and setting them into relation, the flow properties at the probe tip can be concluded. For a five-hole probe, the pressures $p_1 - p_5$ are recorded and post-processed. Both, pitch α and yaw β, angles (see figure 5) can be resolved. To gather the calibration data set, different angle combinations and free-stream velocities are set in the free-jet wind tunnel. Figure 6 shows an exemplary calibration grid for a multi-hole pressure probe. For each calibration velocity, several hundreds or sometimes more than a thousand angle combinations are calibrated. The maximal calibration angle of a five-hole probe, and hence its reconstruction range, is near $\pm\, 60^\circ$.

Non-dimensional calibration coefficients can be calculated with the acquired pressures, which form the basis for the interpolation. The interpolation routines can be divided into global or local interpolations, depending on whether all calibration points or only points in the surroundings with similar calibration coefficients should be used. In the local interpolation method, the calibration data is divided into a low- and a high-angle regime, see [22]. The pressure port with the highest measured pressure determines the set of calibration coefficients used for reconstruction. In the event that multiple pressure ports see similar pressures within a given range, overlap segments are defined where the coefficients are calculated for each dominant pressure port. For the low-angle regime, where the central port p_1 measures the highest pressure, the coefficients are defined as follows:

$$b_\alpha = \tfrac{1}{\bar{q}}(p_3 - p_2) \tag{19}$$

$$b_\beta = \tfrac{1}{\bar{q}}(p_4 - p_5) \tag{20}$$

$$A_t = \tfrac{1}{\bar{q}}(p_1 - p_t) \tag{21}$$

$$A_s = \tfrac{1}{\bar{q}}(p_t - p_s) \tag{22}$$

$$\textit{with} \qquad \bar{q} = p_1 - \tfrac{p_2+p_3+p_4+p_5}{4} \tag{23}$$

$\bar{q}$ denotes the pseudo dynamic pressure, which is used to non-dimensionalize the coefficients. In the high-angle regime, where one of the circumferential ports p_i records the highest pressure, the coefficients read:

$$b_\theta = \tfrac{1}{\bar{q}}(p_i - p_1) \tag{24}$$

$$b_\phi = \tfrac{1}{\bar{q}}(p^+ - p^-) \tag{25}$$

$$A_t = \tfrac{1}{\bar{q}}(p_i - p_t) \tag{26}$$

$$A_s = \tfrac{1}{\bar{q}}(p_i - p_s) \tag{27}$$

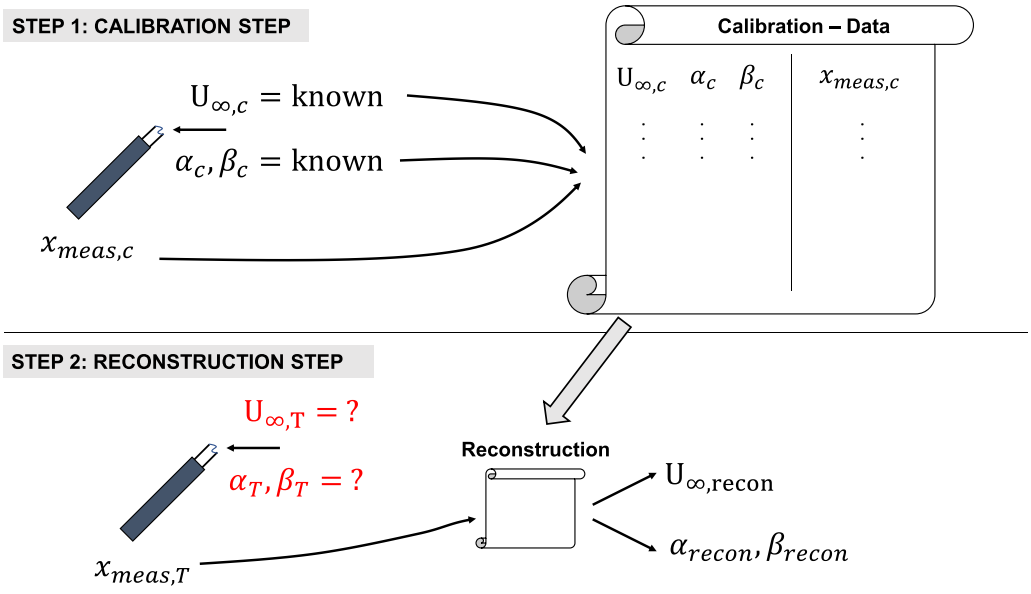

Figure 3. Calibration and reconstruction of aerodynamic probe data.

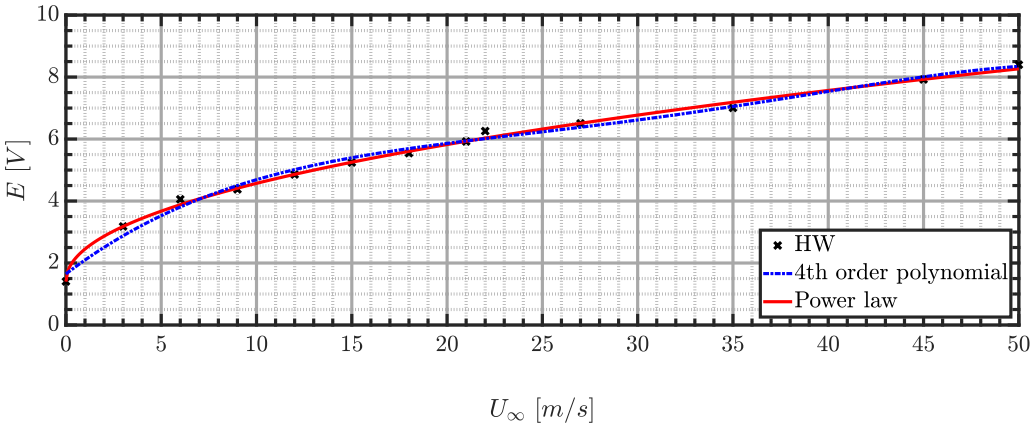

Figure 4. Example of a single-wire calibration.

$$\text{with} \qquad \bar{q} = p_i - \frac{p^+ + p^-}{2} \tag{28}$$

Hereby, p^+ and p^- denote the pressures at the circumferential pressure ports in clockwise and counter-clockwise direction.

During the reconstruction, the test point pressure data vector $\mathbf{p}_T$ is recorded. The subscript T indicates the values at the test point. The non-dimensional coefficients $b_{\alpha,T}$, $b_{\beta,T}$ or $b_{\theta,T}$, $b_{\phi,T}$ for low and high angle regimes are calculated as defined above. In the following step the quantities $A_{t,T}$, $A_{s,T}$ and α_T, β_T or θ_T, ϕ_T are determined by the interpolation algorithm as functions of $f(b_{\alpha,T}, b_{\beta,T})$ or $f(b_{\theta,T}, b_{\phi,T})$. Furthermore, the Mach number M and the deduced velocity magnitude U are calculated as a function of p_t and p_s. The velocity components can be expressed by using the flow angles α and β.

4. Exploitation of gaussian process regression for the calibration of aerodynamic probes

In this section, the findings from section 2 on the fundamentals of Gaussian process regression are applied to calibration data of aerodynamic probes. Using an introducing example in the following section 4.1, the procedure of the Gaussian process regression for the reduction in the number of the calibration points will be demonstrated, see figure 7. Thereby, the application of the GPML Matlab-toolbox implementation by Rasmussen and Nickisch [23] and the choice of the parameters will be discussed. In section 4.2, single-wire CTA calibration data are examined and the applicability of Gaussian process regression to real aerodynamic probe data is shown. As a final demonstration of the approximation technique for aerodynamic probe data, the more complex calibration of a five-hole pressure probe is explained (see section 4.3).

4.1. An introducing example

In this introducing example, the Gaussian process regression procedure from the flow chart in figure 7 is explained step by step using generically generated data. After starting the GPML Matlab toolbox, the available calibration data are read in first.

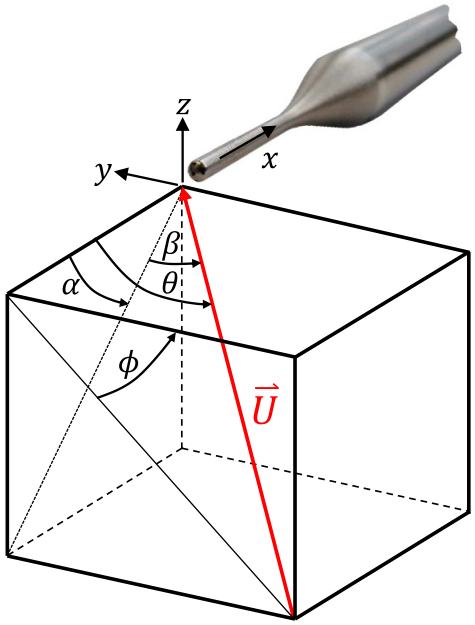

Figure 5. Interchangeable coordinate system: α-β and θ-ϕ.

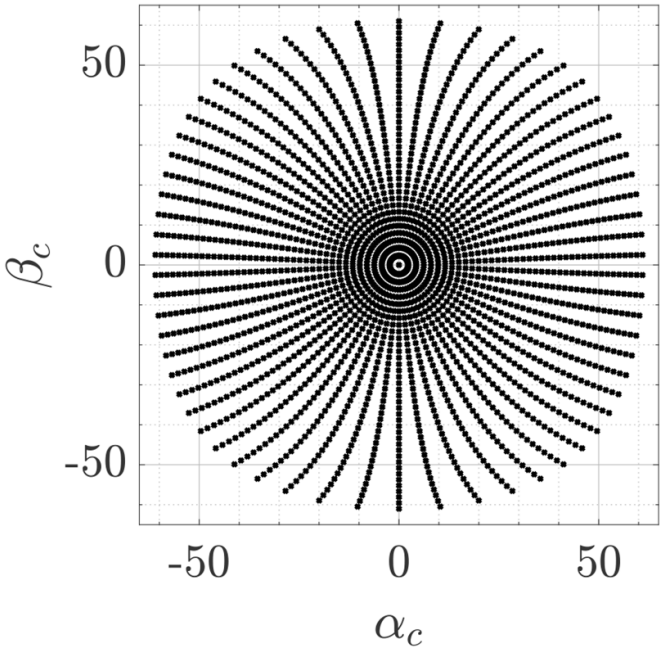

Figure 6. Exemplary calibration grid for a multi-hole pressure probe.

Here, the ten different input data sets are displayed in figure 8 (left). Since the number of input data points is small, the normal $\mathcal{GP}$ approach is applied. A squared exponential kernel function and the Gaussian likelihood formulation is chosen for inference. The prior $\mathcal{GP}(0,k)$ is now initialized with the initial hyperparameters in table 1, and thereafter, a posterior $\mathcal{GP}$ is trained with the input data (see figure 8 (right)). In the optimization step, the hyperparameter vector $\boldsymbol{\theta}$ is optimized by maximizing the log marginal likelihood as described in section 2.2. The optimized values in table 1 show that the initially

Table 1. Prior and optimized hyperparameters for the squared exponential kernel function in the example test case.

	Initial hyperparameter hyp	Optimized hyperparameter hyp_{opt}
σ_l	0.1	2.27
σ_f	0.1	1.61
σ_n	0.1	$2.2 \cdot 10^{-3}$

chosen values vary widely from the optimized hyperparameters. The location of the first supporting point, viz. the location of the first point to be calibrated in the new probe calibration, is determined. This can be done manually or e.g. by choosing the location of the highest predictive output variance, which is available as an output vector of the *gp*-routine. At this point, newly calibrated points of the probe under investigation are added to the $\mathcal{GP}$ regression approach. This is done in a while loop: as long as the termination condition is not fulfilled, an updated conditional $\mathcal{GP}$ is formed with the available supporting points from the new calibration and new locations for further supporting points are determined. If the termination condition is reached, a final $\mathcal{GP}$ is formed with all newly calibrated supporting points. The results of the last step serves as a new calibration curve for the probe and can be used for post-processing or visualization. In figure 9, the *gp*-routine outputs of the first three iterations and the final iteration are visualized. Besides the mean and the standard deviation of the updated $\mathcal{GP}$s, the test curve, which represents the probe calibration curve to be approximated, and the supporting points are shown.

Already after two iterations, the output of the $\mathcal{GP}$ is close to the function to be approximated y_{test}. After five iterations, the termination condition selected here is reached and the final $\mathcal{GP}$ is calculated. The $\mathcal{GP}$-output matches almost exactly the test curve y_{test}.

4.2. Single-wire CTA-probes

In this test case, real aerodynamic probe calibration data of single-wire CTA probes are used. The input data set comprises 13 different single-wire calibrations. Each of the calibrations was conducted separately and is independent of each other. The bridge balancing and setup of the CTA was done in advance and the gain and offset voltages were set, respectively. Furthermore, some calibrations were digitized with an AD-converter analog input voltage range up to 5 V and some with up to 10 V. Furthermore, the maximum calibrated air speed differs between the input data sets. Maximum velocities range from 10 m s^{-1} up to 120 m s^{-1}. Concluding, the input data sets are independent of each other and very heterogeneous.

In the following first part of the hot-wire investigations, the regular $\mathcal{GP}$ regression methodology, as explained in the introducing example shown in figure 7, is applied on the hot-wire data. After first tests, the Matérn 3/2 kernel is chosen for the covariance and the following initial hyperparameters are chosen (see table 2). For the sake of consistency and clarity,

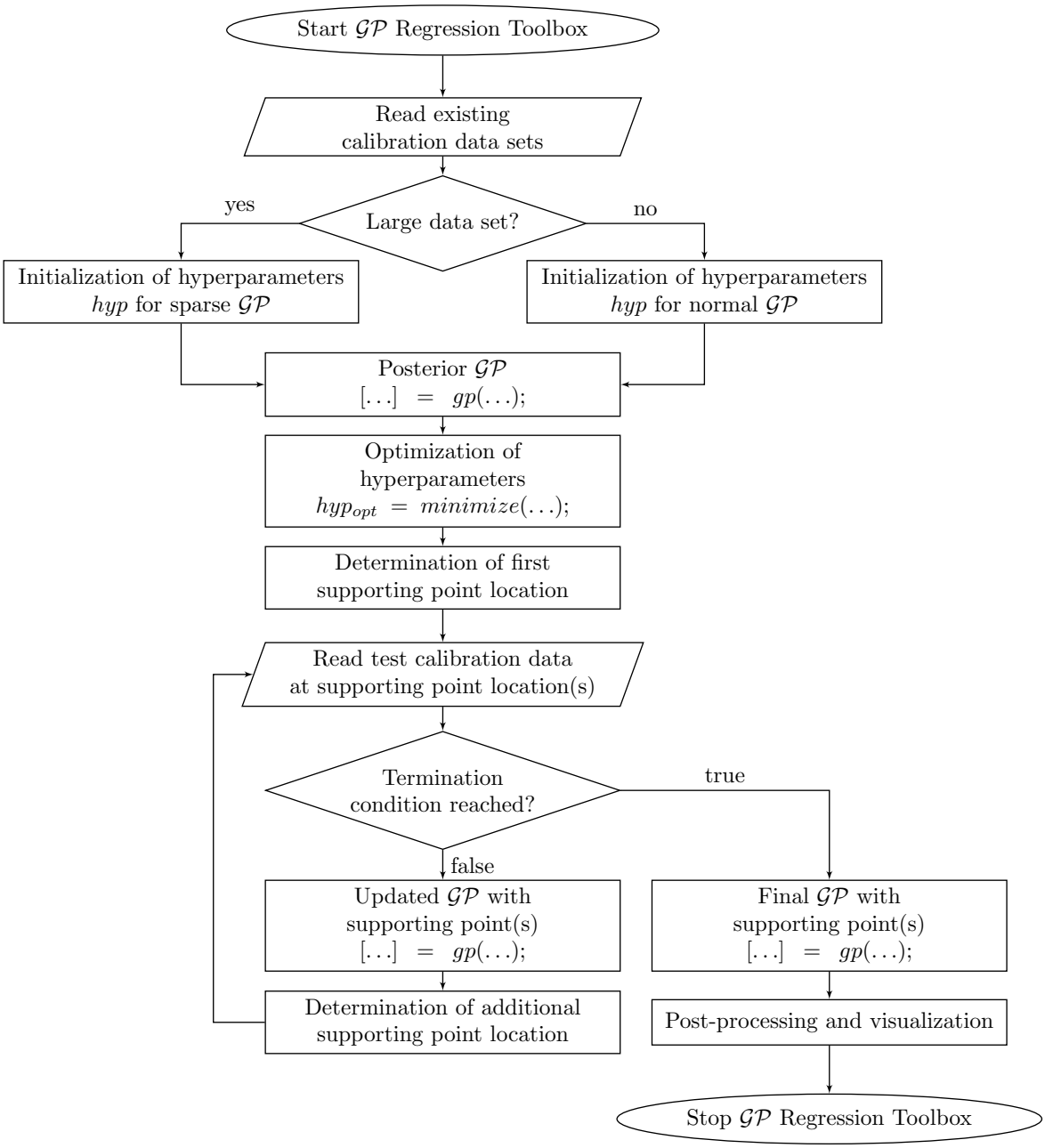

Figure 7. Flow chart of the Gaussian process regression applied on aerodynamic probe calibration data.

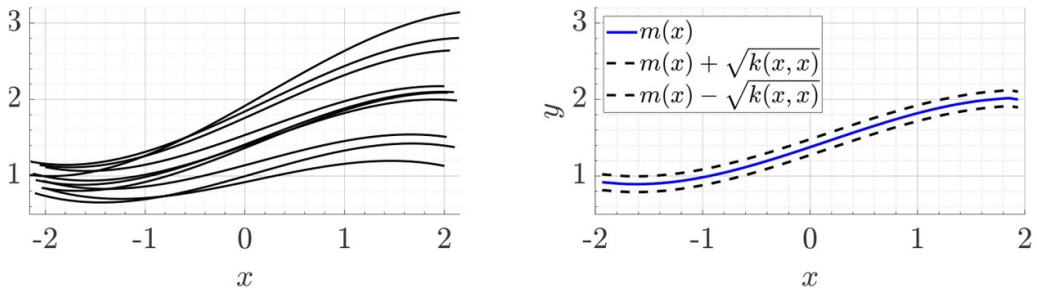

Figure 8. Input data sets for the introducing example (left) and the initial $\mathcal{GP}$ (right).

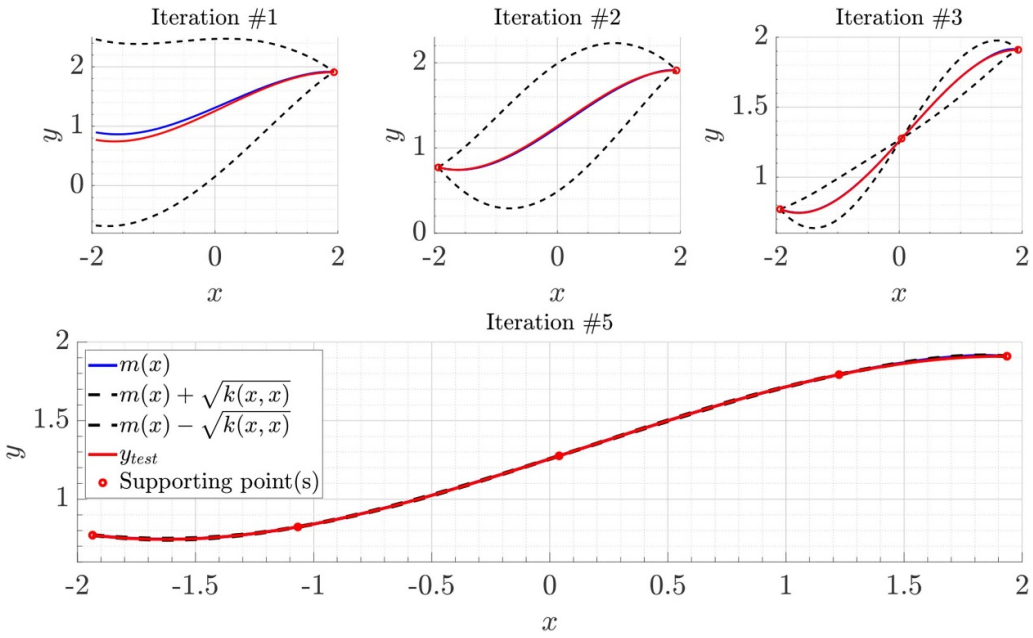

Figure 9. Output of the updated $\mathcal{GP}$s with supporting points in comparison to the test function y_{test} for the first three and the final iteration.

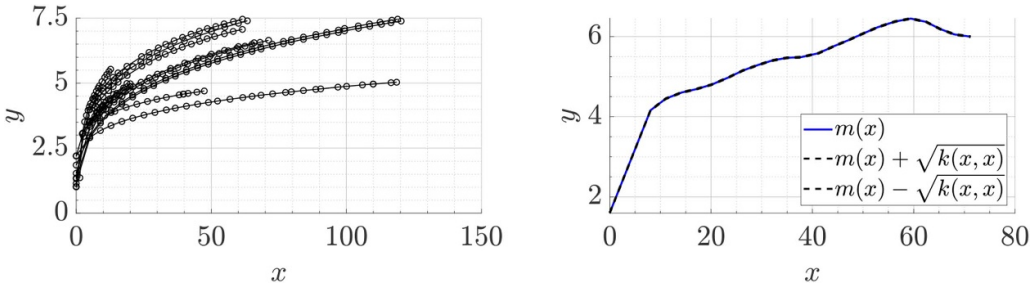

Figure 10. Input data sets for the hot-wire data (left) and the initial $\mathcal{GP}$ (right).

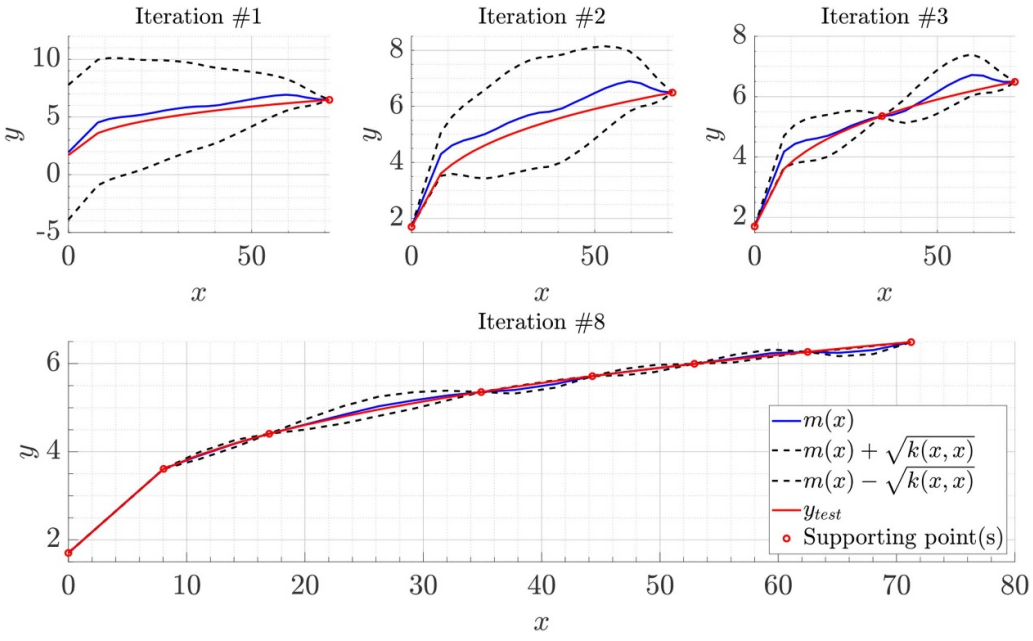

Figure 11. Output of the updated $\mathcal{GP}$s with supporting points in comparison to the test function y_{test} for the first three and the final iteration for the hot-wire data.

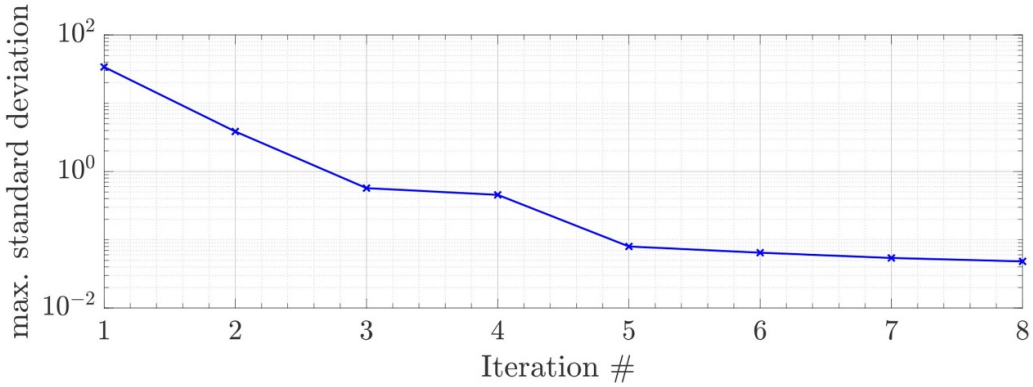

Figure 12. Maximum standard deviation of the $\mathcal{GP}$ after each iteration for the determination of new supporting points.

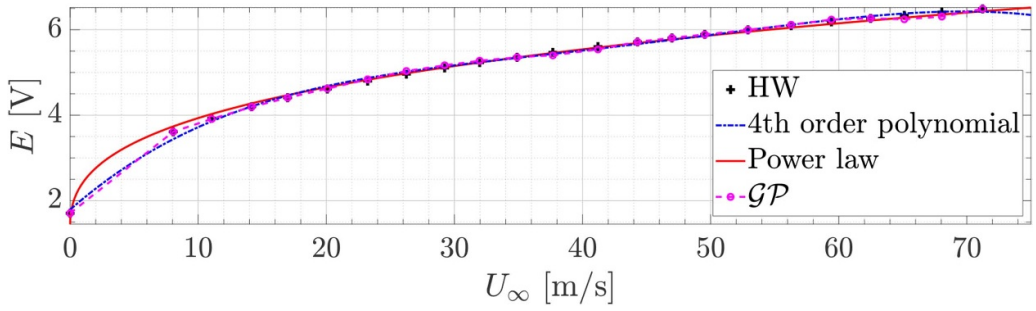

Figure 13. Hot-wire calibration data fitted with a 4th order polynomial and a power law fitting and described by the final $\mathcal{GP}$.

Table 2. Prior and optimized hyperparameters for the Matérn 3/2 kernel function in the hot wire test case.

	Initial hyperparameter hyp	Optimized hyperparameter hyp_{opt}
σ_l	1000	112.96
σ_f	10	8.19
σ_n	$1.0\ 10^{-2}$	$1.5\ 10^{-7}$

the velocity and voltage data are denoted as **x** and **y**, respectively. In figure 10 (left) all calibration data that are used for the determination of the initial $\mathcal{GP}$ (see figure 10 (right)) are shown. Figure 11 shows the updating process of the $\mathcal{GP}$ regression routine for various iterations. After eight iterations, the termination condition is reached. Figure 12 displays the maximum standard deviation of the updated $\mathcal{GP}$ after each iteration. It is used to determine the location of the next supporting point. The relative improvement between the successive steps is decreasing and after the 8th iteration the standard deviation lies below the margin for the termination condition.

In figure 13, the hot-wire test calibration that is to be approximated by the Gaussian process regression is shown. Here, results of both fitting methods, which are described in section 3.1, are displayed alongside the mean of the final updated $\mathcal{GP}$. The free parameters are chosen as $\boldsymbol{\theta}_{poly} = [1.7871,\ 0.2629,\ -8.1602 \cdot 10^{-3}, 1.2661 \cdot 10^{-4},\ -7.1646 \cdot 10^{-7}]$ for the polynomial fitting. With a gradient descent optimization approach, the power law coefficients were set to $\boldsymbol{\theta}_{pow} = [2.0969, 3.7724, 0.5491]$.

In the second part of the hot-wire investigations, the influence of the initial determination of the hyperparameters on the outcome of the Gaussian process regression is studied. This is done in a sampling routine, similar to a Monte-Carlo-method (MCM) simulation. It is determined how many supporting points are needed to reach the determination criterion. Thereby, the three hyperparameters σ_l, σ_f and σ_n are sampled out of three normal distributions $\mathcal{N}_{\sigma_l}(1000, 300)$, $\mathcal{N}_{\sigma_f}(10, 5)$ and $\mathcal{N}_{\sigma_n}(0.01, 0.0001)$, respectively. $N_{MCM} = 10^4$ multivariate samples are drawn and tested. The determination criterion of each of the N_{MCM} $\mathcal{GP}$s is set to a threshold RMS-difference value of $\varepsilon_{rms} = 0.05$ between the updated $\mathcal{GP}$-output and the test hot-wire calibration. Figure 14 shows the resulting number of supporting points needed to reach ε_{rms} for each MCM-sample, as well as the initial and the updated hyperparameters.

The initialized hyperparameters show the expected Gaussian shape, and hence, the assumed number of MCM-samples $N_{MCM} = 10^4$ is appropriate, which is a prerequisite before discussing the output data. In the column for the optimized hyperparameters after the GPML optimization routine, it can be seen that the distributions are not fully Gaussian anymore. The noise hyperparameter σ_n is negligible now, whereas σ_l is distributed around a mean of $\bar{\sigma}_l = 110$ and σ_f around a mean of $\bar{\sigma}_f = 8.2$. Furthermore, it can be seen that for most samples, solely seven to ten supporting points are needed. In comparison to the full calibrations, which frequently comprise

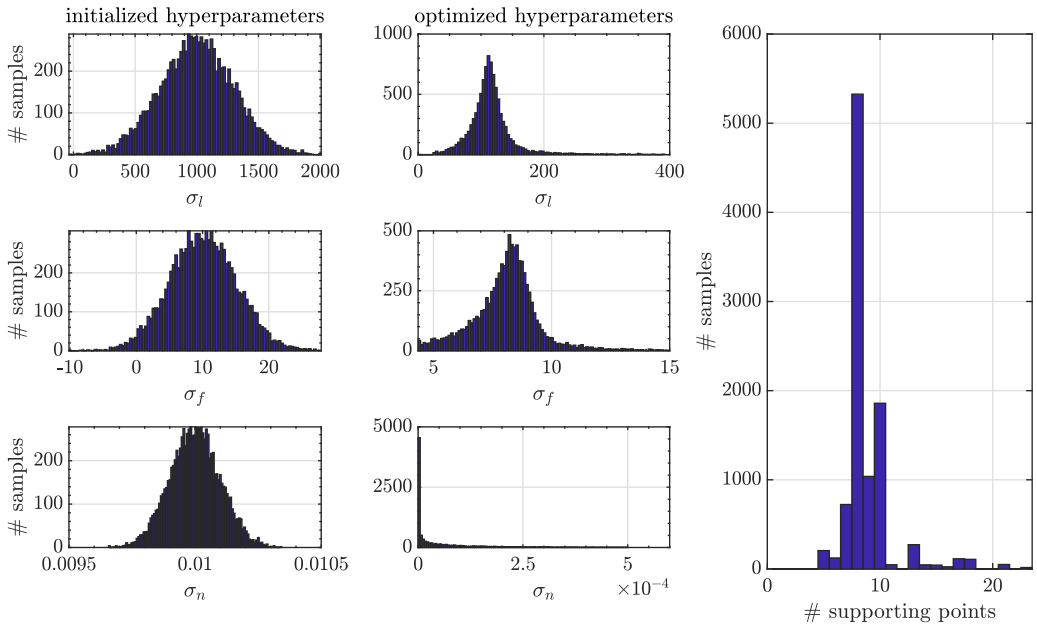

Figure 14. MCM sampling of hyperparameters: initialized (left) and optimized hyperparameters (middle), number of supporting points of $\mathcal{GP}$ for the termination condition (right).

Table 3. Overview of the existing calibration data: probe tip diameter D, calibration Reynolds number Re_D, and Mach number M.

	min(D) [mm]	max(D) [mm]	min(Re_D)	max(Re_D)	min(M)	max(M)	# *probes*
Straight	1.6	6.35	3000	40 000	0.03	0.6	15
L-shaped	1.0	3.2	1000	55 000	0.024	0.95	8
Cobra-shaped	3.0		3000	38 000	0.05	0.6	1
Conical	1.0	3.2	1000	55 000	0.024	0.95	20
Hemispheric	3.0	6.35	3000	28 000	0.03	0.4	4

Table 4. Prior and optimized hyperparameters for the Matérn 3/2 kernel function in the five-hole pressure probe test case.

	Initial hyperparameter *hyp*				Optimized hyperparameter *hyp*$_{opt}$			
	$\mathcal{GP}_\alpha$	$\mathcal{GP}_\beta$	$\mathcal{GP}_{A_t}$	$\mathcal{GP}_{A_s}$	$\mathcal{GP}_\alpha$	$\mathcal{GP}_\beta$	$\mathcal{GP}_{A_t}$	$\mathcal{GP}_{A_s}$
σ_l	50.0	50.0	50.0	50.0	8.06	7.00	7.82	9.20
σ_f	10.0	10.0	10.0	10.0	4.28	4.53	0.21	0.29
σ_n	0.1	0.1	0.1	0.1	$2.55 \cdot 10^{-5}$	$2.06 \cdot 10^{-6}$	$1.59 \cdot 10^{-6}$	$4.02 \cdot 10^{-6}$

up to 30 calibration points, the introduced calibration approach applying a $\mathcal{GP}$ regression algorithm leads to a reduced number of calibration points and hence a reduction in calibration time.

4.3. Five-hole pressure probes

The calibration of five-hole probes results in four calibration surfaces for α, β, A_t and A_s as functions of $f(b_\alpha, b_\beta)$. Hence, the shown results in this chapter are the outcomes of multiple, viz. four simultaneous, $\mathcal{GP}$ regressions. The determination of the supporting points of the updated $\mathcal{GP}$s will be evaluated globally, but the updating of every single $\mathcal{GP}$ itself is handled independently. All existing calibration data sets are read in first. They consist of data of 24 different probes, which are shaped differently. The probe stem shape varies between straight, L-shaped and cobra-shaped probe stems and conical and hemispheric probe tips with varying diameters D are present. The overhang length for the L-shaped probes vary between $(1.5, 9.5)\cdot D$. For some probes, calibration data for different inflow Mach numbers are available. Therefore, 45 input data sets in the Mach number range between $M = (0.024, 0.95)$ are used to train the initial $\mathcal{GP}$. An overview of the different calibration data including the range of diameters D, Reynolds numbers Re_D and Mach numbers M is given in table 3.

When concatenating the input data sets, with $n = 47\,577$ calibration points, the number of points exceeds the limit for the standard $\mathcal{GP}$ regression due to limitation of the necessary $\mathcal{O}(n^3)$ matrix manipulations. For this reason, the sparse approximation with $m = 1681$ locations $(b_\alpha | b_\beta)$ is applied as described in section 2.2 which in turn reduces the costs to $\mathcal{O}(mn^2)$. The Matérn 3/2 kernel is used for the four $\mathcal{GP}$s as

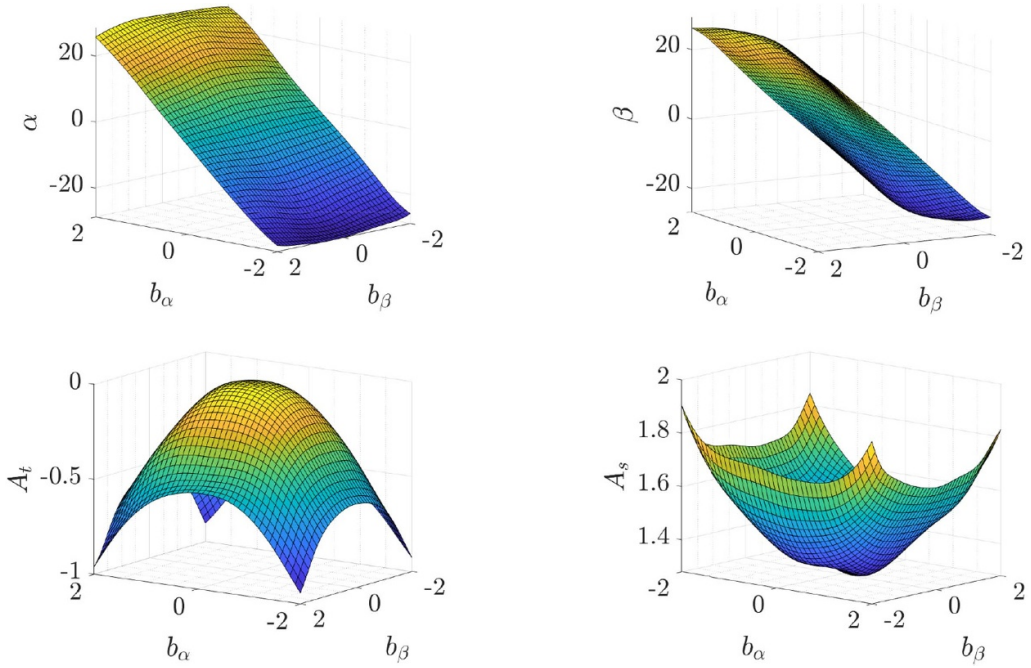

Figure 15. Initial $\mathcal{GP}$s for the four calibration surfaces.

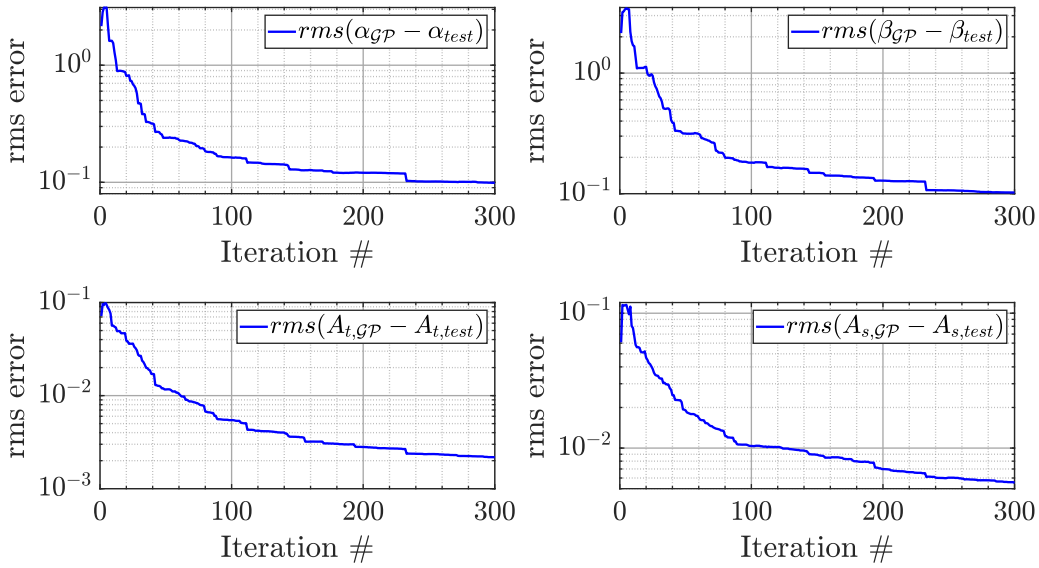

Figure 16. RMS error convergence of the $\mathcal{GP}$ outputs and the full calibration values with increasing iterations.

Table 5. Spatial reconstruction results for the $\mathcal{GP}$ after the 80th iteration compared to the full calibration data.

	$\Delta\alpha$ [°]			$\Delta\beta$ [°]			ΔM [$\cdot 10^{-3}$]		
	maxabs	*rms*	*std*	*maxabs*	*rms*	*std*	*maxabs*	*rms*	*std*
$\mathcal{GP}$	0.41	0.14	0.15	0.27	0.13	0.13	1.07	0.42	0.40
Full calibration	0.23	0.08	0.08	0.26	0.09	0.08	0.63	0.36	0.21

the covariance function and is initialized with the initial hyperparameters in table 4. After initialization, the $\mathcal{GP}$ is updated with the sparse input values. Figure 15 shows the initial $\mathcal{GP}$s for the four calibration surfaces. A visualization of the standard deviation as displayed in the preceding 1D cases is omitted for clearer visualization.

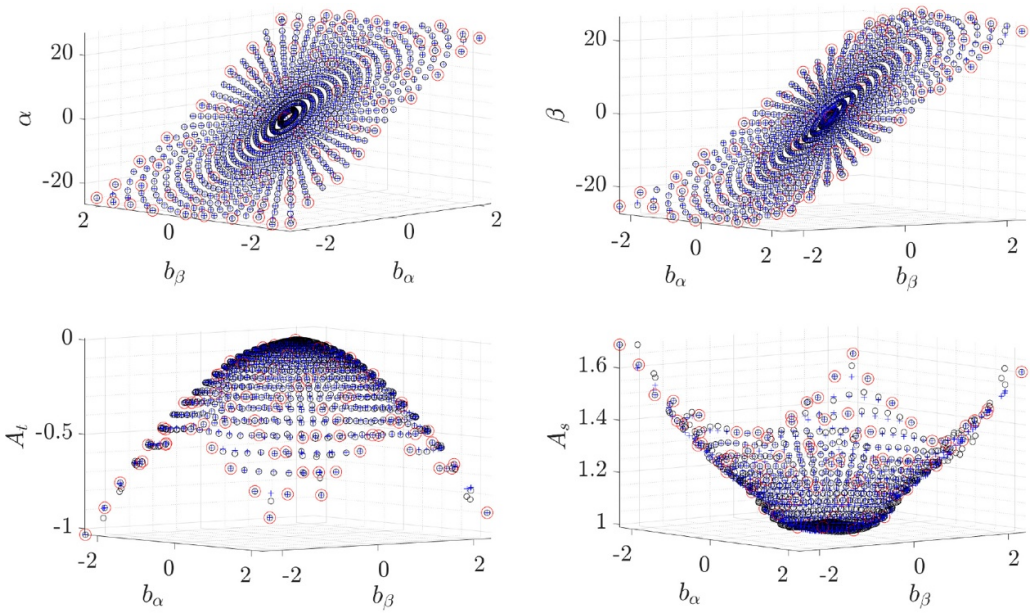

Figure 17. Updated $\mathcal{GP}$s for the four calibration surfaces after the addition of 80 supporting points: +(blue) - $\mathcal{GP}$ output, °(black) - full calibration, ◯(red) - supporting points.

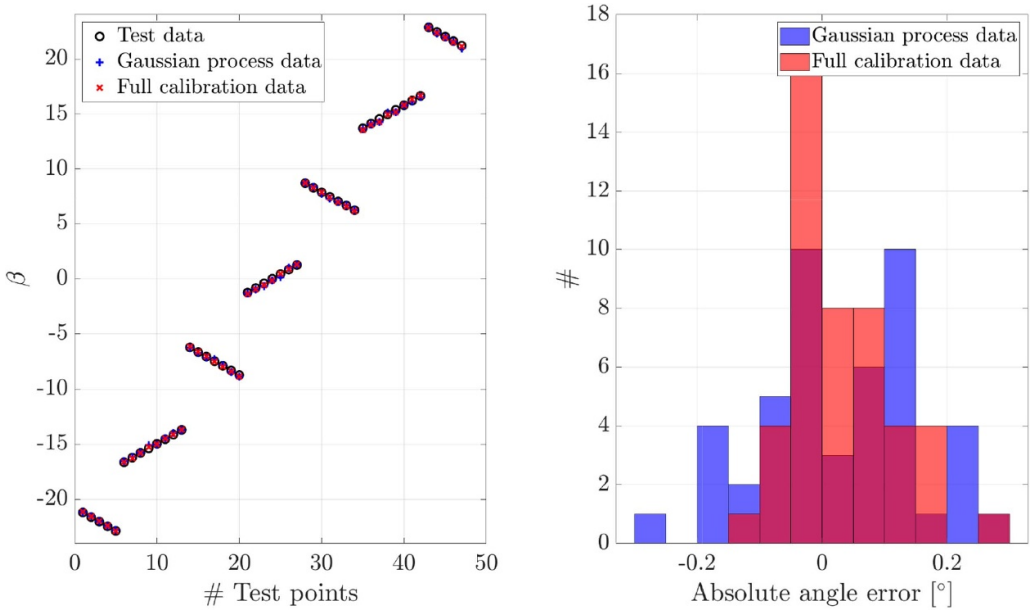

Figure 18. Test point reconstruction of the angle α with the updated $\mathcal{GP}$ after the addition of 80 supporting points compared to the full calibration reconstruction.

In order to better compare the output of the $\mathcal{GP}$ regression, the probe under investigation was fully calibrated beforehand. It is a straight five-hole probe with a hemispheric probe tip with a tip diameter of $D = 3$ *mm*. It was calibrated for three inflow velocities. Two of these calibration data sets are part of the input data sets and the remaining one is the *test* calibration, denoted either as *full* calibration or with the index $^*_{test}$.

In the next step, optimized hyperparameters for the four $\mathcal{GP}$s are found by optimizing the log marginal likelihood. The resulting hyperparamters which remain unchanged during the upcoming updating routine are gathered in table 4 as well. The computational costs for the initialization step and the optimization of the hyperparameters lie in the order of (a few) minutes on a state-of-the-art workstation and, hence, can be considered as negligible in contrast to wind tunnel set-up costs. In the updating procedure, supporting point locations are added to the $\mathcal{GP}$. Due to the fact that four $\mathcal{GP}$s have to be updated simultaneously, a criterion which $\mathcal{GP}$ contributes the next supporting point is defined. For each $\mathcal{GP}$, the location of the maximum standard deviation of the updated $\mathcal{GP}$ normalized by the standard deviation of the first iteration is calculated. Depending which of the four $\mathcal{GP}$s experiences the highest normalized standard deviation, the location of the additional supporting point for the next iteration for all $\mathcal{GP}$s is chosen. A termination criterion stopping the iterative updating

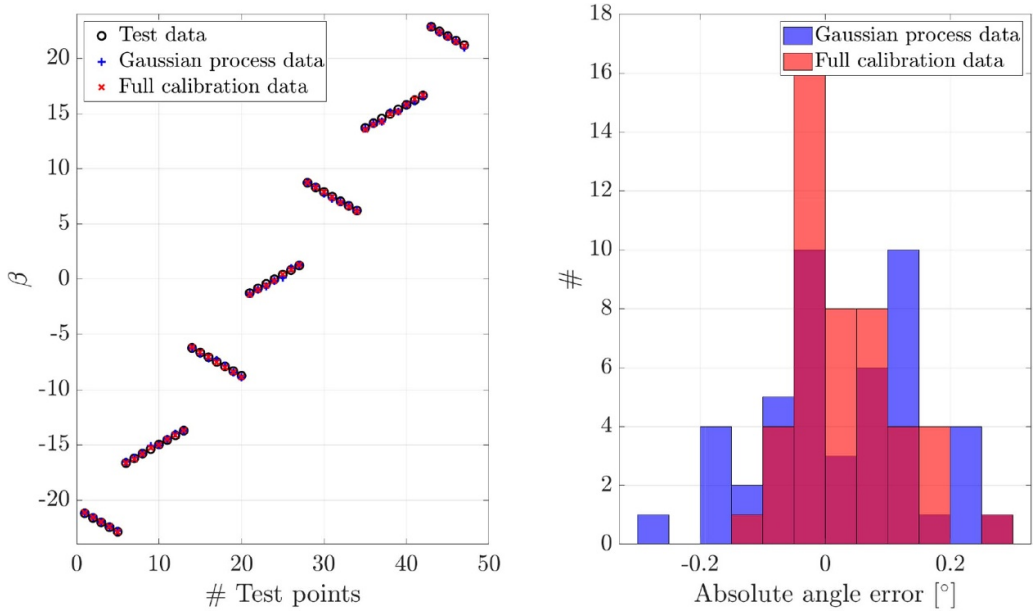

Figure 19. Test point reconstruction of the angle α with the updated $\mathcal{GP}$ after the addition of 80 supporting points compared to the full calibration reconstruction.

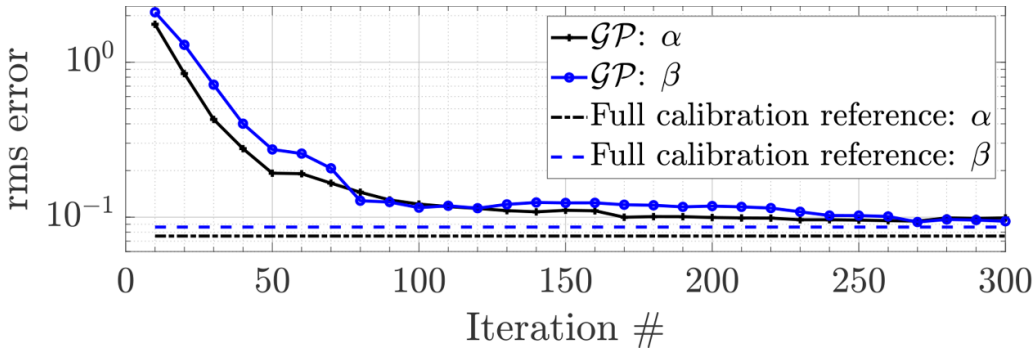

Figure 20. RMS errors of the test point reconstruction of the angles α and β when increasing the number of updating iterations of the $\mathcal{GP}$.

process can be applied. For example, if the maximum normalized standard deviation or the RMS value of the sum of standard deviations for the four $\mathcal{GP}$s falls below a pre-defined margin, the criterion is reached and the solution is converged. Since, in this example, the full calibration for the multi-hole probe was also done in order to compare it to the results of the $\mathcal{GP}$, the number of iteration steps was fixed to 300 for the first investigations. After each iteration, the RMS error between the $\mathcal{GP}$ output data and the full calibration data is displayed in a semi-logarithmic plot in figure 16. When discussing the $rms(\beta_{\mathcal{GP}} - \beta_{test})$ plot, the RMS value reads around 1° for the 10th iteration and drops below 0.2° for around 80 iterations.

Figure 17 visualizes the $\mathcal{GP}$ outputs of the 80th iteration of the four calibration surfaces. Furthermore, the 80 supporting points and the full calibration test surfaces are shown. Visually, there are only very small noticeable deviations in the A_t and A_s plot. The errors between the α and β $\mathcal{GP}$ outputs and the full calibration surfaces seem negligible.

For quantifying the visually perceived deviations in figure 17, a reconstruction of unknown test points is performed in the next step, also known as *generalization*. In this process, 47 test data points measured independently of the determination of the calibration surfaces are post-processed with the final $\mathcal{GP}$ output and the full calibration data. The test points comprise pressure measurements $\mathbf{p}_T$ of different angle combinations at a fixed Mach number of $M = 0.1$. Figure 18 and figure 19 show the results of the post-processing step conducted with the $\mathcal{GP}$ and the full calibration data. Besides a visualization of the reconstructed angles, a histogram shows the absolute angle errors in degrees, calculated with the true angle values set in the calibration wind tunnel as reference values.

Table 5 gives an overview of the quantified results of the reconstruction: apart from the maximum absolute occurring error among the test results *maxabs*, the RMS errors *rms* and the standard deviation *std* are formed across all test points for the angles α and β as well as for the reconstructed Mach number M.

To conclude the investigations on the five-hole probe, a series of reconstructions with different sized $\mathcal{GP}$ models is shown. Thereby, the number of supporting points was

increased in steps of 10 up to 300 supporting points. The reconstruction accuracy for α and β in terms of the RMS error of the $\mathcal{GP}$ is displayed in the semi-logarithmic plot in figure 20. With an increasing number of supporting points, the RMS errors asymptotically approach the reference values of the full calibration reconstruction. After 80 to 100 supporting points, only marginal improvements are noticeable. This leads to the conclusion that with the application of $\mathcal{GP}$ regression, the number of actually measured points to build a calibration surface, capable to reconstruct with almost the same accuracy, can be decreased over one order of magnitude. In the case that lower requirements are made in terms of reconstruction accuracy, the number of supporting points can be reduced by a multiple, furthermore. Hence, calibration set-up costs, expressed by the number or time of measured points, could be reduced in this example by the factor of $F = 1014/80 = 12.68$ for high reconstruction accuracy (angle RMS below 0.15°) and the factor of $F = 1014/40 = 25.35$ for lower reconstruction accuracy (angle RMS below 0.5°).

5. Concluding remarks

In this paper, the application of Gaussian process regression on the calibration of aerodynamic probes is shown. Besides introducing into the theoretical background of the Bayesian statistics approach, the basic ideas in probe calibration methods for CTA and pressure probes are presented. The approach of applying $\mathcal{GP}$ regression to aerodynamic calibration data is introduced in a generic example and shows the potential of the method. The method is tested on two real data sets: the 1D calibration of a single-wire hot-wire probe and the 3D calibration of a five-hole probe. The more challenging task of modeling the four calibration surfaces of the five-hole probe can be performed very accurately with the newly developed $\mathcal{GP}$ methodology, yielding promising results. A reconstruction with the $\mathcal{GP}$ calibration with a twelfth of the calibration points, compared to the full calibration, provides a comparably accurate reconstruction of the test points. Moreover, this procedure can also be performed for probes of different sizes and probe head shapes in a reliable and robust manner. The only requirement for the input data is that they are generated during the calibration of the same type of probe. For example, calibrations of three-hole probes could not be used to generate the $\mathcal{GP}$ for five-hole probes. Finally, the hypotheses presented in the introduction are evaluated: The applicability of Gaussian process regression to aerodynamic calibration data from hypothesis 2 is mainly shown in the introducing example in section 4.1. The flow chart 7 shows the principle procedure of the $\mathcal{GP}$ calibration. Especially in the pressure probe test in section 4.3, hypothesis 1 can be confirmed by training the initial GP with more than 47 000 input data points and combining the similarity of the different probe calibrations. When looking at the results obtained from the 3D calibration of the five-hole probe, the savings potential in calibration time becomes obvious. The prerequisite for achieving this is, obviously, that a sufficiently large input data set of different probes is available, viz. various probe shapes with different tip diameters which are calibrated in a wide Reynolds numbers range. The reduction in the number of calibration points by at least one order of magnitude is demonstrated with comparable reconstruction accuracy. A speed-up factor of $F > 10$ can be realized for multi-hole pressure probes. In future developments, the $\mathcal{GP}$ calibration module is planned to be further refined, optimized and extended to other types of probes.

Acknowledgments

The authors would like to thank the company Vectoflow GmbH for providing the multi-hole pressure probe calibration data of numerous different probes. Furthermore, the authors would like to thank the electricians of the Chair of Aerodynamics and Fluid Mechanics, Luigi Findanno and especially Hans-Gerhard Frimberger. Last, we are grateful for the contributions of our colleague Vladislav Rosov.

ORCID iD

Florian M Heckmeier https://orcid.org/0000-0002-1130-729X

References

[1] Rediniotis O K and Vijayagopal R 1999 Miniature multihole pressure probes and their neural-network-based calibration *AIAA J.* **37** 666–74
[2] Johansen E S, Rediniotis O and Jones G 2001 The compressible calibration of miniature multi-hole probes *Trans. of the ASME* **123** 128–38
[3] Heckmeier F M, Iglesias D, Kreft S, Kienitz S and Breitsamter C 2019 Development of unsteady multi-hole pressure probes based on fiber-optic pressure sensors *Eng. Res. Express* **1** 025023
[4] Gelman A, Carlin J B, Stern H S and Rubin D B 2014 *Bayesian Data Analysis* Chapman and Hall/CRC 3rd ed Boca Raton
[5] Rasmussen C E and Williams C K I 2006 *Gaussian Processes for Machine Learning* (MIT Press) Cambridge, MA
[6] Chilés J and Delfiner P 2012 *Geostatistics: Modeling Spatial Uncertainty Wiley Series in Probability and Statistics* (New York: John Wiley & Sons, Ltd) ISBN 9781118136171
[7] Krause A, Singh A and Guestrin C 2008 Near-optimal sensor placements in Gaussian processes: Theory, efficient algorithms and empirical studies *J. Mach. Learn. Res.* **9** 235–84
[8] Pandit R K, Infield D and Carroll J 2019 Incorporating air density into a Gaussian process wind turbine power curve model for improving fitting accuracy *Wind Energy* **22** 302–15
[9] Chen T 2007 Calibration of spectroscopic sensors with gaussian process and variable selection *IFAC Proc. Volumes* **40** 137–42
[10] García-Ruiz R A, Blanco-Claraco J L, López-Martínez J and Callejón-Ferre J 2019 Uncertainty-aware calibration of a hot-wire anemometer with Gaussian process regression *IEEE Sens. J.* **19** 7515–24
[11] Agrawal R, Whalley R D, Ng H C H, Dennis D J C and and Poole R J 2019 Minimizing recalibration using a non-linear regression technique for thermal anemometry *Exp. Fluids* **60** 116

[12] Rasmussen C E 2004 *Gaussian Processes in Machine Learning* (Berlin: Springer) pp 63–71
[13] Bishop C M 2006 *Pattern Recognition and Machine Learning* (Berlin: Springer)
[14] Nocedal J and Wright S J 2006 *Numerical Optimization* (New York: Springer) 2nd ed
[15] Quinonero Candela J and Rasmussen C 2005 A unifying view of sparse approximate Gaussian process regression *J. Mach. Learn. Res.* **6** 1935–59
[16] Snelson E and Ghahramani Z 2006 Sparse gaussian processes using pseudo-inputs *Advances in Neural Information Processing Systems 18* (Cambridge, MA: MIT Press) pp 1257–64
[17] Rasmussen C E and Nickisch H 2018 The GPML Toolbox version 4.2 *Tech. Rep.*
[18] Bearman P 1969 *Corrections for the Effect of Ambient Temperature Drift on Hot-Wire Measurements in Incompressible Flow* Teddington: National Physical Laboratory(NPL)
[19] Hultmark M and Smits A J 2010 Temperature corrections for constant temperature and constant current hot-wire anemometers *Meas. Sci. Technol.* **21** 105404
[20] Hewes A, Medvescek J I, Mydlarski L and Baliga B R 2020 Drift compensation in thermal anemometry *Meas. Sci. Technol.* **31** 045302
[21] Bruun H H 1995 *Hot-Wire Anemometry: Principles and Signal Analysis* (Oxford: Oxford University Press)
[22] Heckmeier F M, Iglesias D, Kienitz S and Breitsamter C 2019 An innovative development of a five-hole pressure probe for highly unsteady flow phenomena *ASME Turbo Expo 2019: Volume 6: Ceramics; Controls, Diagnostics and Instrumentation; Education; Manufacturing Materials and Metallurgy* ASME
[23] Rasmussen C E and Nickisch H 2010 Gaussian processes for machine learning (GPML) toolbox *J. Mach. Learn. Res.* **11** 3011–15